

A Lagrangian framework for analyzing microstructural level response of polymer-bonded explosives

Ananda Barua and Min Zhou¹

G.W. Woodruff School of Mechanical Engineering, Georgia Institute of Technology,
801 Ferst Dr N.W., Atlanta, GA 30332-0405, USA

E-mail: abarua@gatech.edu and min.zhou@gatech.edu

Received 30 December 2010, in final form 27 April 2011

Published 13 June 2011

Online at stacks.iop.org/MSMSE/19/055001

Abstract

A cohesive finite element method (CFEM) framework for quantifying the thermomechanical response of polymer-bonded explosives (PBXs) at the microstructural level is developed. The analysis carried out concerns the impact loading of HMX/Estane at strain rates on the order of 10^4 – 10^5 s⁻¹. Issues studied include large deformation, thermomechanical coupling, failure in the forms of microcracks in both bulk constituents and along grain/matrix interfaces, and frictional heating. The polymer matrix is described by a thermo-elasto-viscoelastic constitutive formulation, accounting for temperature dependence, strain rate sensitivity and strain hardening. The HMX crystals are assumed to be elastic. The CFEM framework allows the contributions of individual constituents, fracture and frictional contact along failed crack surfaces to heating to be tracked and analyzed. Digitized micrographs of actual PBX materials and idealized microstructures with Gaussian distributions of grain sizes are used in the analysis. The formation of local hot spots as potential ignition sites is primarily due to the viscoelastic dissipation in the matrix in early stages of deformation and frictional heating along crack surfaces in later stages of deformation. The framework is a useful tool for the design of energetic composites and the results can be used to establish microstructure–response relations that can be used to assess the performance of energetic composites.

(Some figures in this article are in colour only in the electronic version)

1. Introduction

Polymer-bonded explosives (PBXs) are a class of composites consisting of explosive crystals and a soft polymeric binder. They are used in a wide variety of civil and military applications such as detonators and solid rocket propellants. The content of explosives in the

¹ Author to whom any correspondence should be addressed.

composites varies between 60% and 95% by mass, similar to that in pressed explosives. The mechanical properties of PBXs are strongly influenced by the binder whose elastic modulus is approximately three to four orders of magnitude lower than that of the granules. This allows the binder to deform and absorb most of the mechanical work imparted to the composites during impact loading. Hence, the binder provides structural toughness to and reduces the impact sensitivity of the composites. This attribute also allows PBXs to be pressed and machined to desired shapes and sizes.

PBXs may be subject to dynamic loading with stresses on the order of several GPa for durations of 10–100 ms. Responses under such conditions are complex since they are inherently non-scalable. Consequently, current PBX designs are primarily based on empirical trial and error which is time consuming and material specific. It is highly desirable to quantify the conditions that lead to reaction initiation of the energetic composites as they undergo mechanical, thermal and chemical changes upon impact loading. In particular, the establishment of processing–microstructure–response relations would allow systematic design and exploration of processing routes and material configurations that are tailored to specific applications [1].

In the last two decades, a significant amount of research has focused on experimental characterization of PBXs and their constituents. Palmer and Field [3] studied the mechanical deformation of β -HMX. Subsequently, Palmer *et al* [4] analyzed the distribution of stress, failure strength and fracture behavior of PBXs of different compositions. Several other studies have focused on the characterization of heterogeneous microstructures (e.g. [5, 6]), fracture and deformation (e.g. [7–10]), influence of temperature and strain-rate (e.g. [11, 12]) and correlation between microstructure and fracture behavior (e.g. [2]). Wiegand *et al* [13] investigated the effect of confinement on behavior and reported significantly higher elastic modulus and flow stress at higher confinement levels. Siviour *et al* [14] argued that the fracture of crystals is unlikely to produce significant heating due to their low fracture toughness. Menikoff *et al* [15], on the other hand, reasoned that frictional dissipation along fractured surfaces might lead to high temperature rises, especially under conditions of significant confinement.

A significant amount of work has been done on the shock compression of heterogeneous materials using Eulerian-formulation-based approaches. Benson *et al* [16] carried out 2D hydrocode simulations to analyze the densification of granular HMX. Austin *et al* [17] studied the shock compression of microstructures with aluminum–iron oxide (thermite) particles in a polymer binder. Baer [18] studied the consolidation, deformation and reaction of HMX crystals using highly resolved 3D simulations. Their results suggest that the stress state in a heterogeneous material shows large fluctuations and localization of heating or formation of ‘hot spots’ is due to inelastic deformation and interaction between crystals which cannot be modeled using a continuum level approach. Menikoff [19, 20] studied pore collapse, another important mechanism responsible for the formation of hotspots.

So far, Eulerian simulations have not attempted to capture fracture and interfacial debonding between binder and grains and fracture of grains. These failure mechanisms cause overall loss of strength and lead to frictional dissipation at fractured surfaces. Lagrangian formulations can more effectively track interfaces [21, 22]). Such a method has been used by Banerjee *et al* [23] to study the effect of grain/binder debonding on the elastic modulus of a glass-Estane PBX simulant. Wu *et al* [24] used a rate-dependent viscoelastic cohesive zone model for the binder and a continuum damage model for the HMX grains to simulate the response of PBX 9501 in Brazilian compression tests. Results from these studies suggest that fracture of grains and grain/binder debonding play important roles in the failure of PBXs.

Simulations with explicit account of microstructural features and processes allow the delineation of the influences of different microstructural attributes, deformation and failure mechanisms and heat generation mechanisms. In particular, shear banding, interfacial

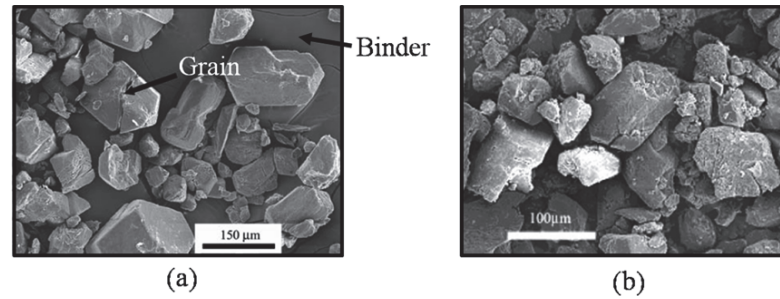


Figure 1. Morphologies of HMX grains in a pressed PBX, (a) before impact loading and (b) after impact loading [2]. With kind permission from Springer Science + Business Media: Chen P W, Huang F L and Ding Y S 2007 *J. Mater. Sci.* **42** 5272.

debonding, collapse of voids and fracture of grains can be resolved using a Lagrangian framework. These processes initiate at different stages of a dynamic loading event and proper resolution of them requires experimental calibration of a model.

In this study, a cohesive finite element method (CFEM)-based framework is developed and used, accounting for microstructure and the thermal-mechanical processes outlined above. Such a framework has been extensively used to study a wide variety of issues related to delamination and fracture such as tensile decohesion [25], quasi-static crack growth [26], ductile fracture [27, 28], dynamic fracture [29], dynamic fragmentation [30, 31], delamination in composites [32, 33] and microstructural fracture [34]. Here, cohesive elements are embedded throughout the microstructure, along all elements boundaries, as in [34]. This approach allows arbitrary fracture paths and patterns inside each phase and along the interfaces between the phases to be resolved. This form of CFEM obviates the need for criteria for fracture initiation and propagation but requires the model to satisfy limitations on mesh density and cohesive stiffness [35]. Contact and friction between failed crack surfaces are accounted for, allowing heating due to interfacial sliding to be analyzed along with heating due to bulk constitutive inelasticity. The framework entails a fully coupled thermal-mechanical formulation, therefore, the interactions between the mechanical process of dynamic deformation and failure and the thermal process of heat generation and conduction are resolved. A range of actual and idealized microstructures with varying attributes are considered in order to establish relationships between microstructural features such as grain size, distribution and contiguity and stress–strain response, failure and heating. The objective is to formulate microstructure–properties relations in a manner that lends them to the design and development of PBXs with tailored property attributes.

2. Microstructure of PBX

As shown in figure 1, a typical PBX microstructure consists of explosive particles such as HMX or RDX in a soft polymer matrix. The preparation of PBXs involves mixing, in a solvent, the explosive powder, binder and a small amount of additives such as plasticizers and oxidizers. Once the mixture has dried up, it is compressed at an elevated temperature to increase density and in turn the explosive output of the charge. A detailed description of the preparation of PBX 9501 may be found in [36]. Explosive crystals have multifaceted irregular shapes and are distributed randomly. Most PBX composites are essentially isotropic at scales above several interparticle distances.

Grain morphology, distribution and volume fraction play an important role in determining the explosive output and the thermomechanical response of PBXs. Figure 2(a) shows the digitized image of an actual PBX microstructure. Variations of this microstructure with a range of grain volume fraction (η) between 0.42 and 0.82 are shown in figures 2(b)–(f). Morphological parameters for these random microstructures are coupled and their effects cannot be easily analyzed independently. To delineate the influence of phase attributes such as phase size, phase arrangement, phase shapes and phase size distribution, a series of idealized microstructures with systematically varying arrangement, size and shape of HMX grains are generated and used in the numerical simulations. These idealized microstructures consists of

- (a) randomly distributed diamond-shaped grains (figure 3) with normal distributions of grain size (figure 4) and grain volume fraction $\eta = 0.42$ – 0.74 ;
- (b) randomly distributed circular grains (figure 5(a)) with a normal distribution of grain size (figure 6(a)) and grain volume fraction $\eta = 0.69$ and
- (c) randomly distributed circular grains (figure 5(b)) with a bimodal distribution of size (figure 6(b)) and grain volume fraction $\eta = 0.69$.

The grain size distributions for the microstructures in figures 2–3 and figure 5(a) are monotonic, with means between 148 and 255 μm and standard deviations between 47.13 and 121.35 μm . The grain size distribution for the microstructure in figure 5(b) is bimodal, with two mean values, one at 294 μm and the other at 98 μm . The standard deviations for these two peaks are 50 μm and 16 μm , respectively, as shown in figure 6(b). The bimodal distribution is an effective means to increase the proportion of explosives in a composite. Packing densities up to 99% of the theoretical maximum density (TMD) have been achieved using this approach [4]. The more intimate packing enhances the interactions between the particles and affects the thermomechanical responses of the compact. This microstructure allows the issue of packing intimacy to be analyzed.

Together, the microstructures discussed above allow the effects of volume fraction (figure 3), particle shape (figures 4(b) and 5(a)) and particle arrangement (figures 5(a) and (b)) to be characterized.

3. Finite-deformation viscoelastic model for the binder

The binder considered is a commercially available polymer known as ESATNE 5703 and used in explosive PBX 9501. It has a glass transition temperature (T_g) of -40°C . The composition and mechanical properties of plasticized Estane can be found in [12, 37]. This material is viscoelastic, with properties sensitive to both strain rate and temperature. Table 1 lists the properties of Estane at $T = 296\text{ K}$, $\varepsilon = 10\%$ and $\dot{\varepsilon} = 2200\text{ s}^{-1}$. Below T_g , Estane is rather brittle and fractures easily; while above T_g , it is ductile. Following the generalized Maxwell model (GMM) in [38], we use a 22-element Prony series to characterize the variation of the shear modulus G of the binder with relaxation time. The bulk modulus, K , of the polymer is assumed to be a constant, as in [24, 38]. The generalized stress–strain relation for a Maxwell model in the current configuration can be expressed in the integral form

$$\sigma(t) = \int_0^t 2G(\tau - \tau') \frac{\partial \varepsilon^D}{\partial \tau'} d\tau' + \int_0^t K(\tau - \tau') \frac{\partial \varepsilon^H}{\partial \tau'} d\tau', \quad (1)$$

where σ represents the Cauchy stress, ε^D and ε^H refer to the deviatoric and hydrostatic portions of the Eulerian strain tensor, and t and τ refer to the physical and reduced times, respectively. The shear modulus G is assumed to vary with the reduced or relaxation time τ according to a

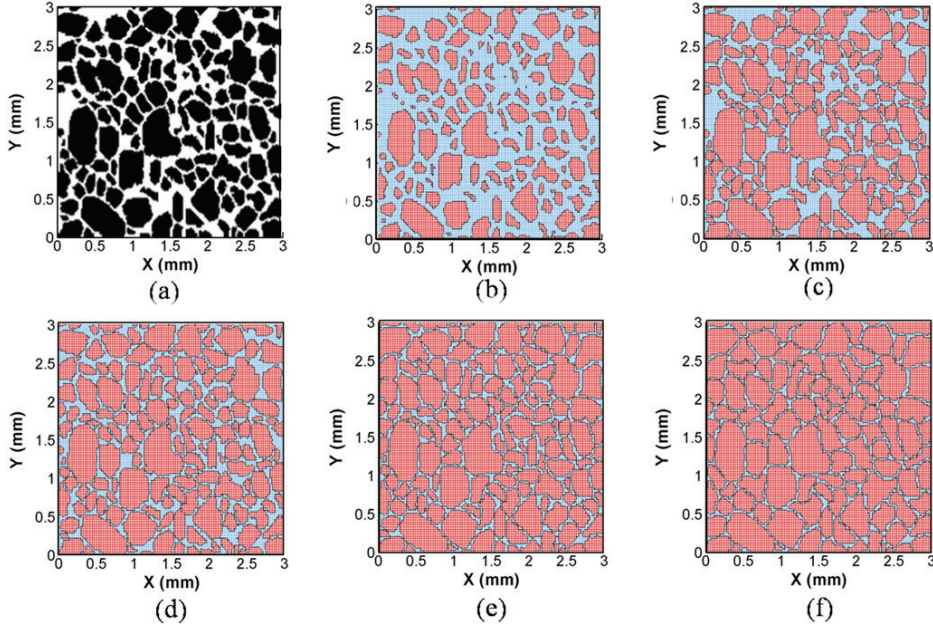


Figure 2. (a) Digitized image of a PBX microstructure from [14] and variations with grain volume fractions of (b) 0.42, (c) 0.64, (d) 0.69, (e) 0.77 and (f) 0.82. Reproduced with permission from the Royal Society: Siviour *et al* 2008 *Proc. R. Soc. A* **464** 1229.

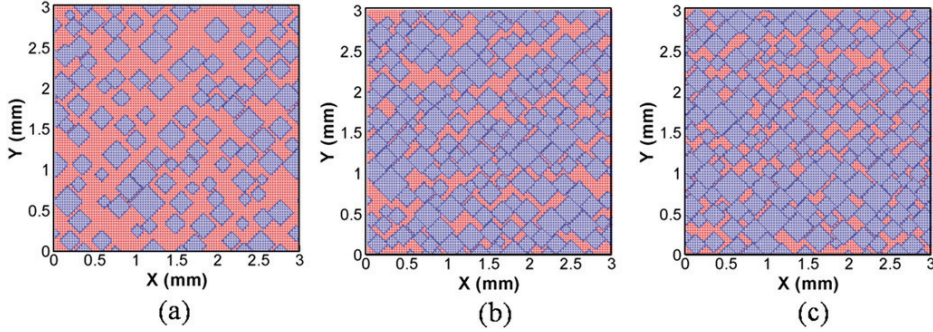


Figure 3. Idealized microstructures with different grain volume fractions, (a) $\eta = 0.42$, (b) $\eta = 0.69$ and (c) $\eta = 0.74$.

Prony series formulation [38] of the form

$$G(\tau) = G_{\infty} + \sum_{i=1}^{N_p} G_i e^{-\frac{\tau}{\tau_i^p}} = G_0 \left(g_{\infty} + \sum_{i=1}^{N_p} g_i e^{-\frac{\tau}{\tau_i^p}} \right), \quad (2)$$

where $G_0 = G_{\infty} + \sum_{i=1}^{N_p} G_i$ and represents the instantaneous shear modulus at reference temperature T_0 , G_{∞} represents the steady-state shear modulus, $g_i = G_i/G_0$ is the relative modulus of the i th term, N_p represents the number of terms in the Prony series and τ_i^p are the relaxation times.

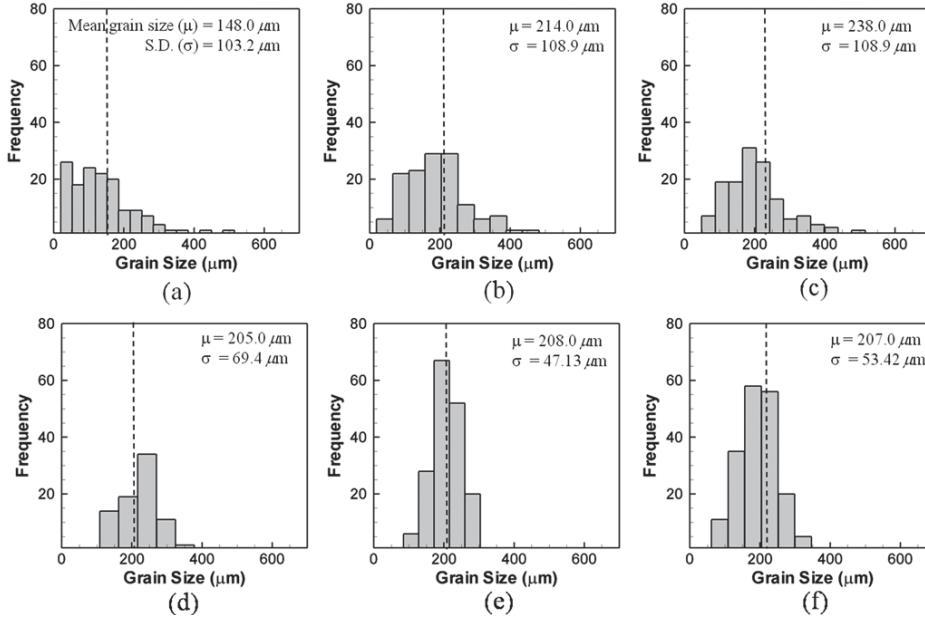


Figure 4. Grain size distributions for the digitized microstructures in figure 2 ((a) $\eta = 0.42$, (b) $\eta = 0.69$, (c) $\eta = 0.77$) and the idealized microstructures in figure 3 ((d) $\eta = 0.42$, (e) $\eta = 0.69$ and (f) $\eta = 0.74$.)

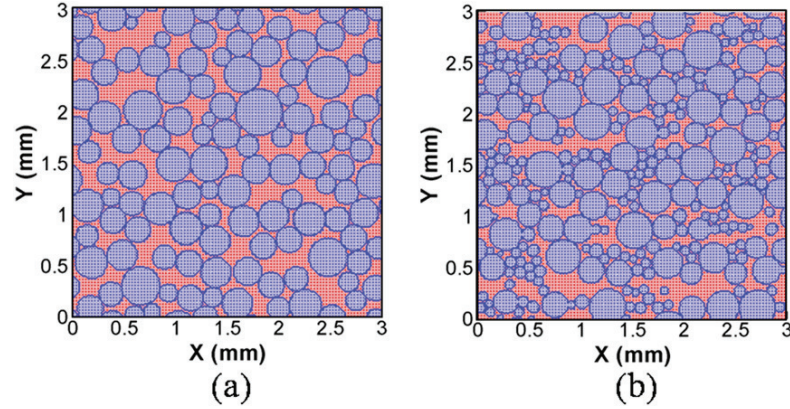


Figure 5. Idealized microstructures with $\eta = 0.69$ (a) monomodal and (b) bimodal distributions.

The modulus of a viscoelastic material at a given strain level is a function of time and temperature. A convenient and appropriate way to describe the dual dependence is to use time-temperature superposition to generate master curves with a shift factor A_T . The time-temperature superposition principle states that the viscoelastic behavior at one temperature can be related to that at another temperature by a change in time scale. The reduced τ time is related to the physical time t via

$$d\tau = \frac{dt}{A_T(T(t))}. \quad (3)$$

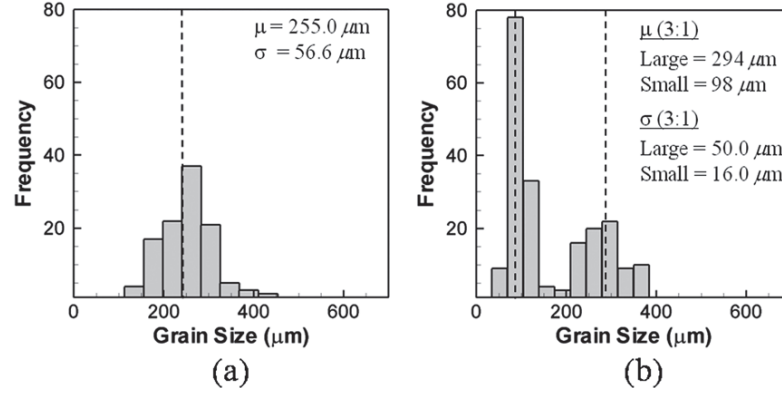


Figure 6. Grain size distributions for idealized microstructures in (a) figure 5(a) and (b) figure 5(b).

Table 1. Material parameters for HMX and Estane.

Material Property	HMX	Estane ($T = 296$ K, $\varepsilon = 10\%$, $\dot{\varepsilon} = 2200$ s $^{-1}$)
Young's modulus	25 325.0 MPa	0.77 MPa (Loading modulus [12])
Density	1.58 g cm $^{-3}$	0.90 g cm $^{-3}$
Specific heat	1254.0 J kg $^{-1}$ K $^{-1}$	1500 J kg $^{-1}$ K $^{-1}$
Poisson's ratio	0.250	0.499

Here, A_T is a shift function which depends on the current temperature T and a reference temperature T_0 . In this paper, a Williams–Landell–Ferry (WLF) shift function is used, i.e.

$$-\log A_T = \frac{C_1(T - T_0)}{C_2 + (T - T_0)}. \quad (4)$$

Here, $C_1 = 6.5$ and $C_2 = 120$ K are constants and $T_0 = 292$ K [38]. Equation (4) describes the equivalent isothermal difference in strain rate between two experiments performed at the same strain rate, one at the reference temperature T_0 and the other at an elevated temperature T . The finite strain viscoelasticity formulation used here is similar to that in [39]. The Jaumann rate of Kirchhoff stress is obtained from the rate of deformation D through

$$\hat{\tau} = \hat{\tau}^H + \hat{\tau}^D = L : D, \quad (5)$$

where L is the isotropic elastic modulus of the binder in the form of

$$L = \frac{E}{1 + \nu} \left(II + \frac{\nu}{1 - 2\nu} I \otimes I \right) \quad (6)$$

and $\hat{\tau}^H$ and $\hat{\tau}^D$ refer to the hydrostatic and deviatoric parts of $\hat{\tau}$, respectively. Also, II is the fourth-order identity tensor, I is the second-order identity tensor, and $I \otimes I$ denotes the tensor product of two tensors. Since the variation of shear modulus G only affects the deviatoric portion of the stress, $\hat{\tau}$ can be rewritten as

$$\hat{\tau} = \left(1 - \sum_{i=1}^{N_p} \alpha_i g_i \right) \hat{\tau}^D + \hat{\tau}^H, \quad (7)$$

where $\alpha_i = 1 - (\tau_i / \Delta\tau)(1 - \gamma_i)$ and $\gamma_i = e^{-(\Delta\tau/\tau_i)}$, with $\Delta\tau$ being the increment of the reduced time τ during the current time step. Substitution of equation (5) into equation (7)

yields the deviatoric part of the Jaumann rate of the Kirchhoff stress as

$$\hat{\tau}_{\text{new}}^{\text{D}} = \left(1 - \sum_{i=1}^{N_p} \alpha_i g_i \right) \cdot (\mathbf{L} : \mathbf{D})^{\text{D}}. \quad (8)$$

The above equation can be further simplified using the instantaneous shear modulus G_0 as

$$\hat{\tau}_{\text{new}}^{\text{D}} = \left(1 - \sum_{i=1}^{N_p} \alpha_i g_i \right) \cdot 2G_0 \mathbf{D}^{\text{D}} = 2G_0 \mathbf{D}^{\text{D}} - 2G_0 \sum_{i=1}^{N_p} \alpha_i g_i \mathbf{D}^{\text{D}}. \quad (9)$$

The first term in the above relation represents the instantaneous elastic response and the second term represents the viscous response. This allows the deviatoric part of the Kirchhoff stress to be updated. Note that the hydrostatic part is unaffected by the viscous strain and, therefore, can be updated using

$$\hat{\tau}^{\text{H}} = (\mathbf{L} : \mathbf{D})^{\text{H}}. \quad (10)$$

Finally, the rate of viscous dissipation can be calculated as the scalar product of the average Kirchhoff stress and the viscous strain rate for each time step. This energy dissipation is manifested as temperature rises in the binder phase. The model parameters are calibrated using experimental data reported in [12] through direct simulations of the experiments.

4. Constitutive model for HMX grains

In this analysis, HMX (octahydro-1,3,5,7-tetranitro-1,3,5,7-tetrazocine) granules are the explosive content. Depending on the temperature and pressure, HMX can have four different forms, α , β , γ and δ , with β being the most stable under ambient conditions. The α phase has a limited domain of stability from 376 to 435 K [40]. As temperature is increased beyond 438 K at atmospheric pressure, the β phase begins to transform to the γ phase. At the melting temperature of 522 K, the γ phase is the most thermodynamically stable form [41].

While considerable information is available regarding the equation of state (EOS) for HMX (see, e.g. [42]), less information is available on constitutive relations. In Eulerian simulations, an EOS is often used for the volumetric part of the response while the deviatoric part is described by an elastic–plastic strength model [16, 19]). Mas and Clemens [43] assumed the grains are elastic–plastic and undergo brittle fracture through crack development. Wu *et al* [24] used a continuum damage model which accounts for the weakening effect of microcracks through decreases in the elastic stiffness.

It is commonly acknowledged that HMX is brittle at ambient pressures [16] and therefore undergo very little plastic deformation. Hence, dissipation associated with plastic deformation is very small compared with the energy spent on fracture development and subsequent frictional dissipation along crack faces. Experiments reveal significant relative displacements of crack surfaces and relative sliding of neighboring grains [44]. Therefore, friction at the contact surfaces is a much more important dissipation and heat generation mechanism for HMX granules than any inelasticity in constitutive response.

In this study, a hyperelastic constitutive formulation is used for HMX, the material properties for which are listed in table 1. The constitutive relation is

$$\mathbf{S} = \frac{\partial W}{\partial \mathbf{E}}, \quad (11)$$

where W is the strain energy density in the reference configuration, $\mathbf{S} = \mathbf{s} \cdot \mathbf{F}^{-\text{T}}$ is the second Piola–Kirchhoff stress and \mathbf{E} is the Lagrangian strain given by

$$\mathbf{E} = \frac{1}{2}(\mathbf{F}^{\text{T}} \cdot \mathbf{F} - \mathbf{I}). \quad (12)$$

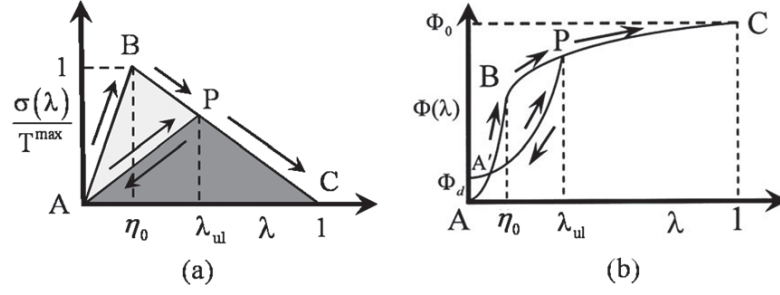


Figure 7. Bilinear traction–separation cohesive law.

In the above formulae, $(\cdot)^T$ and $(\cdot)^{-T}$ denote inverse and inverse transpose, respectively. The strain energy density is taken to be

$$W = \frac{1}{2} \mathbf{E} : \mathbf{L} : \mathbf{E}, \quad (13)$$

where \mathbf{L} is the tensor of isotropic elastic moduli defined in equation (6).

Damage accumulation in the crystals is accounted for via cohesive surfaces embedded throughout the microstructure, as described in the following section.

5. Cohesive finite element framework

In the cohesive model used, the traction \mathbf{T} applied on any cohesive surface is work-conjugate to interfacial separation Δ . Reckoned in the reference configuration, the cohesive law is

$$\mathbf{T}(\mathbf{x}) = \mathbf{T}[\Delta(\mathbf{x})]. \quad (14)$$

Implied here is the assumption that cohesive traction–separation relations are locally determined, i.e. the cohesive traction at one point is fully determined by the separation at the point itself. In the calculations presented in this paper, a bilinear traction–separation law developed by Zhai and Zhou [45] is used. This relation can be regarded as a generalized version of those given by Tvergaard and Hutchinson [26] and Ortiz and Pandolfi [21]. The law is derived from a potential Φ which is a function of the separation vector Δ through a state variable defined as

$$\lambda = \begin{cases} \sqrt{\left(\frac{\Delta_n}{\Delta_{nc}}\right)^2 + \left(\frac{\Delta_t}{\Delta_{tc}}\right)^2}, & \Delta_n \geq 0; \\ \left|\frac{\Delta_t}{\Delta_{tc}}\right|, & \Delta_n < 0. \end{cases} \quad (15)$$

Here, $\Delta_n = \mathbf{n} \cdot \Delta$ and $\Delta_t = \mathbf{t} \cdot \Delta$ denote, respectively, the normal and tangential components of Δ , with \mathbf{n} and \mathbf{t} being unit vectors normal and tangent to the cohesive surface, respectively. Δ_{nc} and Δ_{tc} are the critical normal and shear separations at which the cohesive strength of an interface vanishes under conditions of pure normal ($\Delta_t = 0$) and pure shear ($\Delta_n = 0$) deformation. The specific form of λ aries with the mode of separation. If the value of Δ_n is positive, λ describes the instantaneous state of mixed-mode separations. While if Δ_n is negative (compressive case), λ assumes the value of instantaneous shear separation. This ensures that in the case of compressive loading, the material only fails by shearing.

In order to account for the irreversibility of separations, a parameter $\eta = \max\{\eta_0, \lambda_{ul}\}$ is defined. As illustrated in figure 7(a), η_0 is the initial value of η which defines the stiffness of the original undamaged cohesive surface and λ_{ul} is the hitherto maximum value of λ at

Table 2. Cohesive parameters for the three types of interfaces.

Interface type	Critical separations Δ_n, Δ_r (μm)	Maximum traction T_{max} (MPa)
Grain	5.0	100.0
Matrix	10.0	38.4
Grain–matrix interface	4.62	35.0

which an unloading process was initiated. λ_{ul} represents the (reduced) current stiffness of the cohesive surfaces after damage and unloading have occurred. Also, one always has $\eta < 1$. λ_{ul} is the critical level of λ at which σ reaches the reduced strength of the hitherto damaged cohesive surface pair. The cohesive potential is assumed to be of the form derived in Zhai and Zhou [45].

The bilinear cohesive relation between σ and λ is illustrated in figure 7(a) and the variation of Φ is shown in figure 7(b). The value of Φ_0 is set to be equal to the respective critical energy release rate \mathcal{G} of the particular fracture surface pair (within a HMX granule, inside the ESTANE binder and along a HMX-ESTANE interface). Experimental values of \mathcal{G} , when available, are used to guide the determination of the cohesive parameters. The values of \mathcal{G} for the binder and interface are taken from Tan *et al* [46]. The cohesive parameters used for the three types of interfaces are listed in table 2.

Under compression, penalty traction is used to apply sufficient normal traction on the corresponding node pairs to strongly discourage interpenetration of cohesive surfaces. Specifically, the penalty traction is of the form

$$T_n = T_n^{\text{max}} \exp\left(\frac{\Delta_n}{\Delta_{\text{nc}}}\right), \quad \text{for } \Delta_n < 0. \quad (16)$$

This penalty traction is applied as long as λ is less than 1 for the pair of surfaces. Once $\lambda \geq 1$, i.e. the cohesive element has failed, a contact algorithm (for both free and fractured surfaces) described in the next section is used to prevent interpenetration and account for interfacial friction.

As analyzed in Tomar *et al* [35], there is an issue of cohesive-surface-induced stiffness reduction associated with this type CFEM approach when a finite initial stiffness is used in the cohesive law. This issue is addressed by the use of a sufficiently large initial cohesive stiffness ($\eta_0 = 0.001$) and a finite element size of $30 \mu\text{m}$. These choices satisfy the solution convergence criterion in Tomar *et al* [35] for this type of CFEM models.

6. Contact and friction algorithm

A robust contact algorithm is required to properly account for the interactions between initial boundaries and surfaces that arise out of fracture and debonding inside the material. An algorithm similar to that in Camacho and Ortiz [30] is developed and used. This algorithm works in two steps, the first step involves the detection of potential contact surfaces and the second step involves the application of penalty forces to prevent interpenetration.

Potential contact surfaces include initial free surfaces/boundaries and fractured surfaces. The latter are created when failure of a cohesive surface pair occurs ($\lambda = 1$). The algorithm treats all free surface segments as potential contact surfaces. For each surface segment, a contact region is defined as the area occupied by all of the adjoining elements. At the beginning of every step, the nodal displacements, velocities and accelerations are predicted assuming no contact has occurred. The new nodal coordinates are employed to check for interpenetration within the contact region. Once interpenetration is detected, penalty forces

are applied normally on the pair of surfaces to set them back into alignment. The Coulomb friction law is used to determine the frictional force between a contacting surface pair and in turn the tangential component of the nodal force vector. Frictional work results in the generation of heat and increases the thermal energy of the nodes on the contact surfaces. The thermal force is distributed between the two surfaces according to [30],

$$\frac{h_1}{h_2} = \sqrt{\frac{k_1 \rho_1 c_1}{k_2 \rho_2 c_2}}, \quad (17)$$

where h_i represents the thermal energy changes, k_i , ρ_i and c_i represent the thermal conductivities, mass densities and the heat specific heats of the two materials ($i = 1, 2$), respectively. To keep track of thermal conduction across adjacent elements, temperature continuity is maintained across every node junction. Since a node pair on the two sides of a cohesive surface pair correspond to the same material point in the reference configuration, a thermal energy averaging scheme is used to evaluate the temperature rise ΔT at each node junction according to

$$\Delta T = \frac{\sum_{i=1}^n h_i}{\sum_{j=1}^n m_j c_j}, \quad (18)$$

where n represents the number of nodes at the node junction, m_j is the lumped mass and c_j is the lumped thermal capacitance of the j th node at the junction.

7. Finite element discretization

The finite element discretization is based on linear-displacement triangular elements arranged in a ‘crossed-triangle’ quadrilateral pattern. Neighboring elements are connected through cohesive surfaces. Thus in the undeformed configuration, the cohesive elements are oriented along four directions, horizontal (0°), vertical (90°) and along the diagonals of the quadrilateral ($\pm 45^\circ$). Finite element discretization of the field equations results and the numerical integration scheme is similar to that in Zhou *et al* [47] and shall not be described here.

8. Loading configurations

A 3 mm square microstructural region initially stress free and at rest is analyzed. This sample size is at least one order of magnitude higher than the length scale of the mean grain size for this type of PBX microstructures and for the microstructures in figures 2–3 and 5, thus giving reasonable representations of the microstructures. The loading configurations in figure 8 are designed to account for a range of loading rates and different load triaxialities. The periodic boundary condition in figure 8(a) and the traction-free boundary condition in figure 8(b) for the lateral sides allow conditions of nominally uniaxial strain (confined, high stress triaxiality) and nominally uniaxial stress (unconfined, low stress triaxiality) to be simulated, respectively. This is a 2D model and the conditions of plane-strain prevail. The velocity boundary condition at the top surface and the fixed displacement boundary condition at the bottom surface allow prescribed deformation rates to be imposed.

9. Model calibration

Depending on temperature and strain rate, the dynamic response of PBXs can vary significantly. For the pure polymeric binder, the viscoelastic response obtained from analytical relations is compared with measured compressive stress-strain ($\sigma - \varepsilon$) response from [12] for a range of

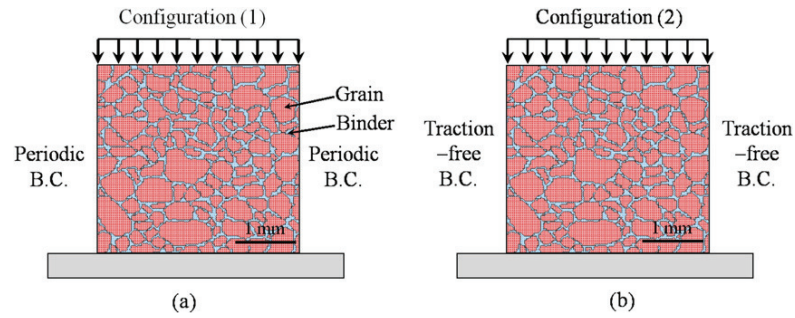


Figure 8. Loading configurations, (a) confined specimen with periodic boundary conditions and (b) unconfined specimen with traction-free boundary conditions on lateral sides.

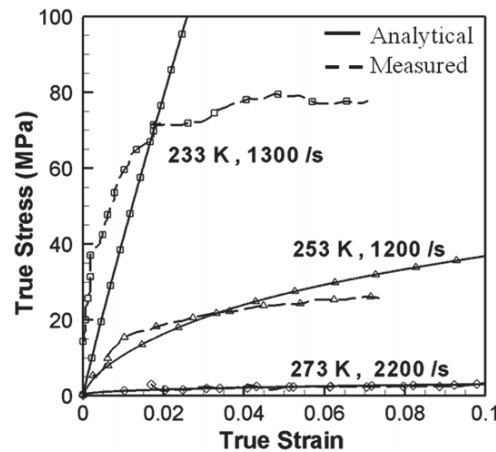


Figure 9. Calculated and measured stress–strain curves for Estane 5703 (experiments by Cady *et al* [12]).

strain rates and initial temperatures (see figure 9). Note that the glass transition temperature for the binder $T_g = 233$ K. For temperatures above the glass transition region, viscoelastic response predicted by the analytical relations is in good agreement with the measured response. However, at temperatures lower than T_g the measured response deviates significantly from the analytical prediction. This is due to damage in the form of brittle fractures decreases the load-carrying capacity of the material. The cohesive traction–separation law for the binder has been calibrated to account for this brittle behavior observed at low temperatures.

The overall response of PBX includes contributions from both the deformation of bulk constituents and the debonding at grain–matrix interfaces. Figure 10 shows a comparison between measured and calculated $\sigma - \epsilon$ responses of PBX 9501 for three initial temperatures from 233 K and 290 K, at a strain rate of $\dot{\epsilon} = 2500$ s⁻¹. The calculations are based on the microstructure shown in figure 2(d). Note that for the calculations at lower temperatures (233 and 273 K), the calculations over-predict the stress in the softening portion of the $\sigma - \epsilon$ response. One possible reason is that at low temperatures, the brittle behavior of the binder causes the $\sigma - \epsilon$ response to be more sensitive to the microstructural heterogeneity. At higher temperatures (293 K) the binder behaves in a more ductile manner and the calculated and

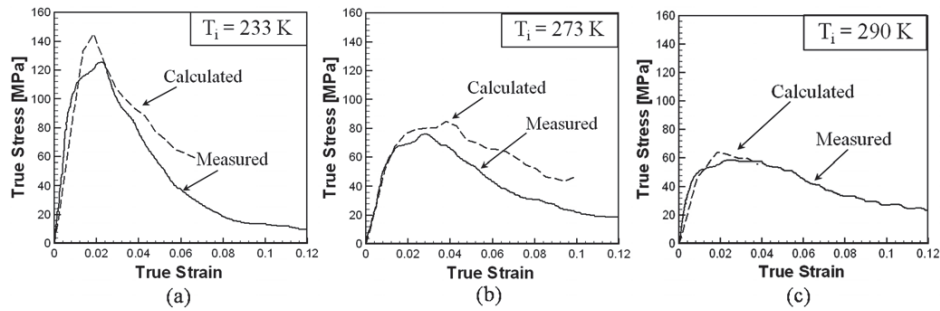


Figure 10. Calculated and measured stress–strain curves for PBX 9501 (experiments by Gray *et al* [11]), $\dot{\epsilon} = 2500 \text{ s}^{-1}$, $\eta = 0.69$.

measured responses are in good agreement with each other. The above comparisons between calculated and experimental results serve as a justification for the bulk constitutive and fracture parameters used in the present analyses.

A convergence study is carried out using meshes with a range of element sizes. The meshes used consist of uniform distributions of ‘crossed-triangle’ squares, each square having four bulk elements. The effect of mesh density or element size is analyzed by varying the number of elements from 10×10^3 to 160×10^3 in the 3 mm square microstructural region. The corresponding element sizes range between 15 and $60 \mu\text{m}$. A set of calculations is performed using the PBX microstructure shown in figure 2(c). The equivalent stress at the location of maximum stress concentration in the microstructure is plotted in figure 11. The relative error in the peak stress is approximately 2.6% of the value for the smallest element sizes. Based on this study, an element size of $30 \mu\text{m}$ is chosen for the calculations presented in this paper.

10. Results and discussions

A systematic analysis is carried out using the actual and idealized PBX micrographs detailed in section 2. The effects of varying microstructural attributes such as volume fraction, grain size distribution and grain phase morphology are analyzed. The analysis enables us to quantify the relationship between the dynamic response of PBXs and their initial compositions and microstructural makeup. The framework is inert, so the effects of possible phase transitions and chemical reactions are not considered. Unless otherwise noted, the imposed boundary velocity at the top surface of the configurations in figure 8 is $V_0 = 50 \text{ ms}^{-1}$ (which gives rise to a nominal strain rate of $\dot{\epsilon} = 16\,667 \text{ s}^{-1}$) with a linear ramp from zero to V_0 in the first $1 \mu\text{s}$ of loading. The initial temperature is $T_i = 300 \text{ K}$. We first use one calculation to illustrate the processes and failure mechanisms captured by the model under the conditions analyzed.

The microstructure used for this calculation is that in figure 2(d) and the loading configuration is that in figure 8(b). Figure 12 shows the distributions of the equivalent stress at times $t = 2.8$ and $4.0 \mu\text{s}$ after the onset of loading. The HMX grains, which are stiffer than the binder, sustain higher stresses. The grains are not uniformly stressed—higher stresses are seen for grains which are part of one of the ‘force chains’, as outlined in figure 12(a). These force chains can be regarded as assemblies of grains positioned such that they support higher levels of compressive and shear stresses [48]. The overall level of stress in the microstructure increases with the progression of deformation until interfacial debonding and transgranular fracture initiate. Figure 12(b) shows the evolution of temperature. Initially, viscous dissipation in

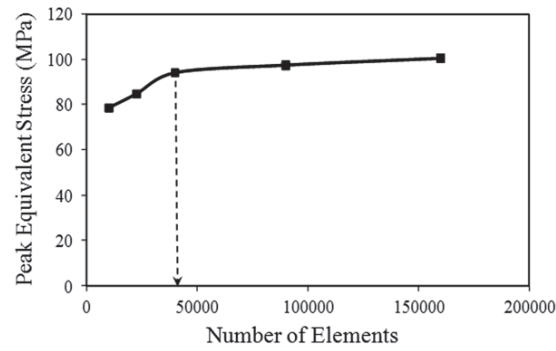


Figure 11. Variation of peak stress with number of elements in the discretized microstructure.

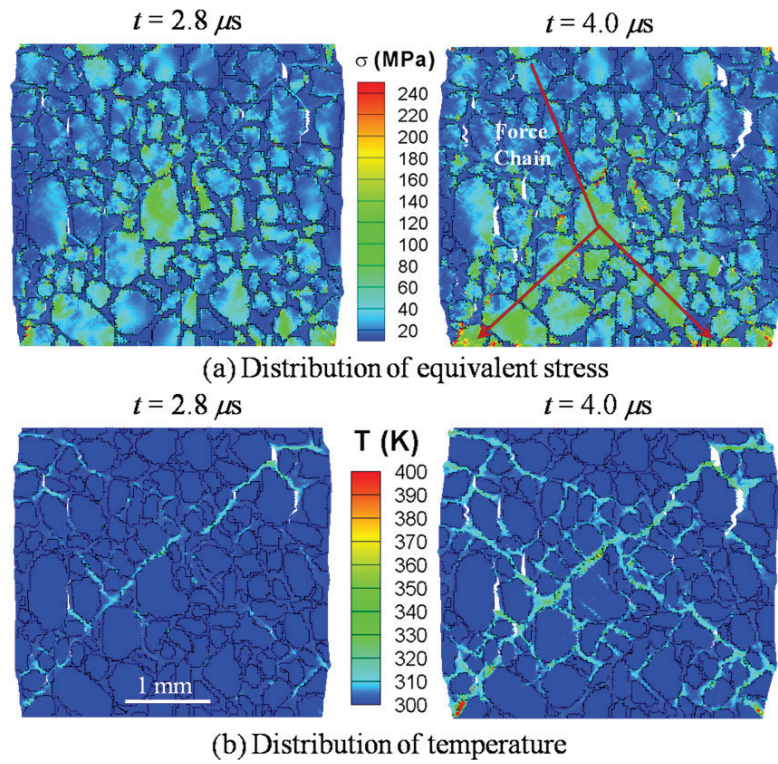


Figure 12. Evolution of (a) equivalent stress and (b) temperature in the microstructure with time for the microstructure in figure 2(d).

the soft binder is primarily responsible for the temperature increase. The hard grains cause more intense deformation in the binder, leading to localized regions of high temperatures. As time progresses, these regions coalesce to form shear bands which tend to extend diagonally through the microstructure, approximately following the direction of maximum shear stress. It is noted that shear bands in the binder alone typically do not generate sufficient heat to cause melting of the HMX grains.

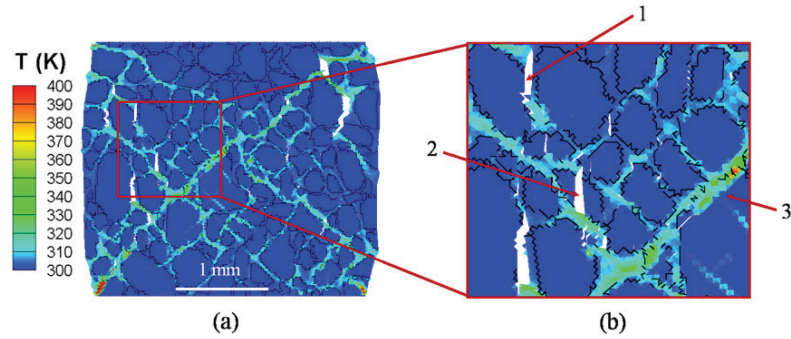


Figure 13. (a) Failure mechanisms in the digitized microstructure with $\eta = 0.69$ shown in figure 2(d) at $t = 4.2 \mu\text{s}$, $T_i = 300 \text{ K}$ and $\dot{\epsilon} = 16\,667 \text{ s}^{-1}$; (b) close-up view of a region of the microstructure showing (1) debonding at grain–matrix interface, (2) transgranular fracture and (3) localized heating due to grain–grain interactions.

The relative motion of grains also activates other energy dissipation mechanisms. Figure 13(a) shows the deformed configuration at $t = 4.2 \mu\text{s}$. A region of this microstructure is shown in figure 13(b) at a higher magnification to highlight the failure mechanisms. Debonding along the relatively weak grain–matrix interface is the primary mode of damage. Such interfacial debonding has also been experimentally observed in experiments at both low and high strain rates (see, e.g., [8, 14]). This form of damage reduces the effective modulus of the over microstructure [23]. At higher levels of nominal strain ($>3\%$), grain–grain interactions occur. The locations where grains come into contact with each other are sites of severe stress concentration, crack development and grain–matrix sliding. Crack formation, sliding and the ensuing frictional dissipation cause more intense heating and higher temperatures. Further deformation lead to transgranular fracture of the grains. Crack development, grain–matrix debonding and transgranular fracture create more surfaces which may come into contact and slide against one another, giving rise to additional frictional dissipation and heating. These processes ultimately can lead to severe heating in the microstructure, resulting in what is known as the hot spots which can cause ignition of energetic materials. Obviously, the interplay between the constituents and interfaces in the microstructure determines the thermomechanical outcome of a dynamic loading event. The outcome defines the ignition sensitivity of the energetic materials.

Figure 14(a) shows the overall stress–strain response corresponding to the results in figures 13 and 14. The stress increases rapidly for strains up to 3%. In this regime, the deformation is primarily accommodated by the softer matrix. Beyond this regime, two competing processes are at work. First, debonding of the grain–matrix interface and transgranular fracture of the grains occur, weakening the load-carrying capacity and contributing to strain softening. This has been observed experimentally by Gray *et al* [11]. Second, as grains are pushed closer, the overall stiffness tends to increase due to enhanced intergranular interactions. These two counteracting mechanisms balance out, leading the stress–strain relation to flatten out in this case.

The time history of energy dissipation in the microstructure is shown in figure 14(b). The profiles for all dissipation mechanism are shown. Viscoelastic dissipation in the binder is the primary dissipation mechanism in early stages of the deformation, as the softer binder absorbs most of the input energy and accommodates most of the imposed deformation. Accordingly, temperature increase occurs primarily in the binder. A portion of the thermal energy is

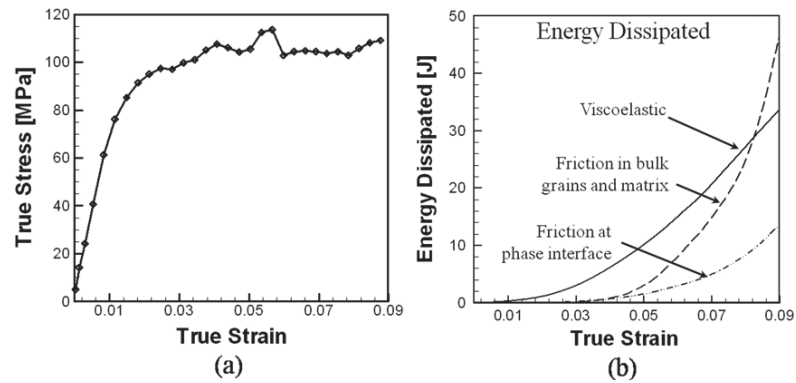


Figure 14. (a) Stress–strain response and (b) time history of energy dissipation in the microstructure shown in figure 2(d) ($\eta = 0.69$, $T_i = 300$ K and $\dot{\epsilon} = 16\,667$ s $^{-1}$).

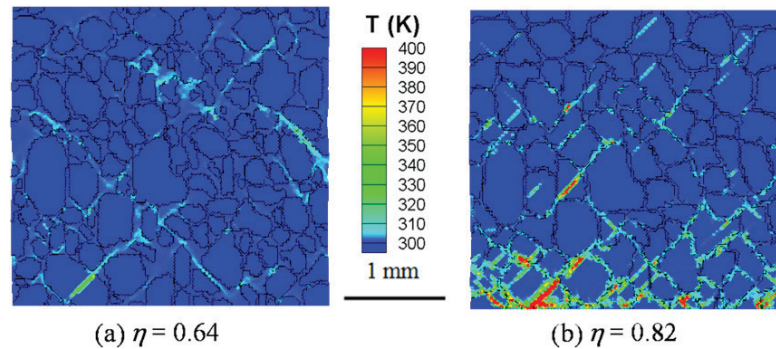


Figure 15. Distributions of temperature at $t = 3.8$ μ s for $T_i = 300$ K and $\dot{\epsilon} = 16\,667$ s $^{-1}$ for two microstructures with different grain volume fractions, (a) $\eta = 0.64$ (microstructure in figure 2(c)) and (b) $\eta = 0.82$ (microstructure in figure 2(f)).

conducted into the grains through the grain–matrix interface. As the overall strain increases, the viscoelastic dissipation continues to increase steadily. Since no fracture occurs in the early stages, frictional dissipation remains zero for strains up to approximately 3% beyond which frictional dissipation initiates in both bulk phases and along the grain–matrix interfaces. The strain at which frictional dissipation initiates also approximately corresponds to the flattening of the stress strain curve, suggesting a transition in heating mechanism from viscoelastic dissipation to frictional dissipation, with the latter occurring between crack surfaces.

10.1. Effect of grain volume fraction

Higher grain volume fractions lead to a larger energy output since the binder is inert. On the other hand, higher grain volume fractions decrease the average thickness of binder between adjacent grains, thereby increasing the reaction initiation sensitivity of the PBX due to more severe binder deformation and grain failure under the same loading condition. To quantify the effect of grain volume fraction on response, a comparative study is carried out using the digitized and idealized microstructures shown in figures 2 and 3. The configuration in figure 8(a) with periodic boundary conditions on the lateral surfaces is used.

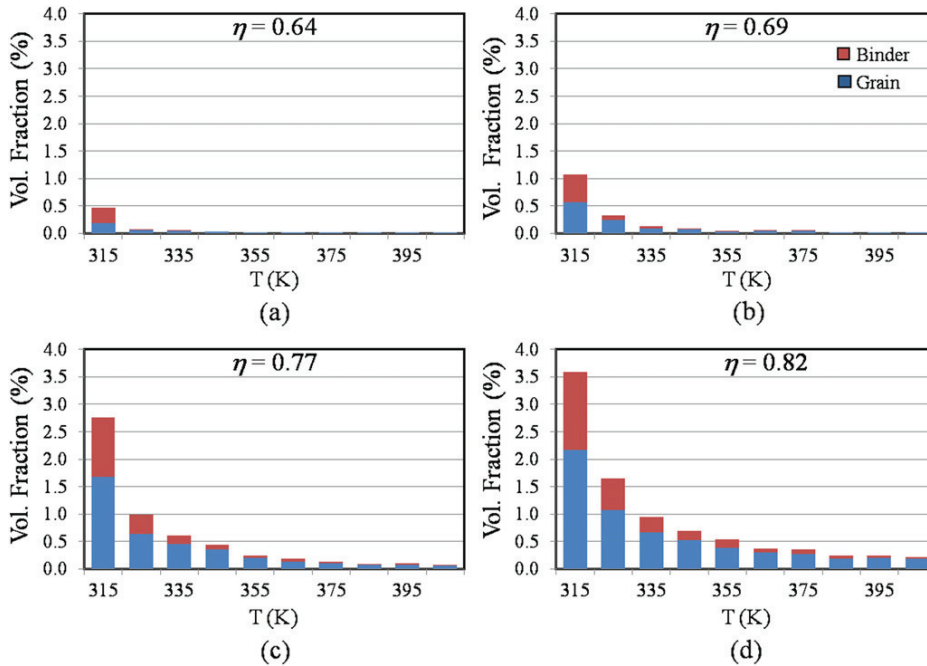


Figure 16. Histograms showing fractions of binder and grains in terms of volume at different temperature ranges for $T_i = 300$ K, $\dot{\epsilon} = 16\,667$ s $^{-1}$ and $\epsilon = 5.5\%$, results for four microstructure compositions (figure 2) are shown.

Figures 15(a) and (b) show the distributions of temperature at an overall strain of $\epsilon = 5.5\%$ for two microstructures, one with a grain volume fraction of $\eta = 0.64$ (figure 2(c)) and the other with a grain volume fraction of $\eta = 0.82$. For the microstructure with $\eta = 0.64$, temperature rises are primarily limited to the binder since essentially no fracture occurs in the grains. In contrast, for the microstructure with $\eta = 0.82$, extensive grain fracture occurs, giving rise to more significant temperature increases in the grains. This is in addition to the higher temperatures in the binder due to more severe deformation. Thus, higher grain contents cause more intense deformation in the binder, hasten the onset of grain–binder interfacial failure and grain–grain interactions, promote grain fracture and increase frictional dissipation, resulting in more pronounced heating under the same loading condition.

The temperature field in figure 15(b) shows more intense deformation and severe heating near the bottom surface. This is due to the fact that the lower boundary is taken as a rigid boundary without transmission of the loading wave into the surrounding medium. Upon impinging on the lower boundary, the incident stress wave is reflected back into the material, subjecting the lower portion of the material to slightly more intense loading.

The temperature rises in the binder and grains are quantified separately in figure 16. The histograms show the volume percentage of each phase having a certain value of temperature after 3.6 μ s of deformation at a strain rate of $\dot{\epsilon} = 16\,667$ s $^{-1}$ (total nominal strain of $\epsilon = 5.5\%$). Clearly, as the grain content (measured by grain volume fraction η) increases heating of both phases in the microstructures intensifies. At the low temperature end (~ 315 – 355 K), the volume percentages for the binder and the grains are similar or of the same order of magnitude. This can be attributed to the lower intensity of heating due to viscoelastic dissipation in the binder and heat conduction into the grains. However, at high temperature rises (> 355 K)

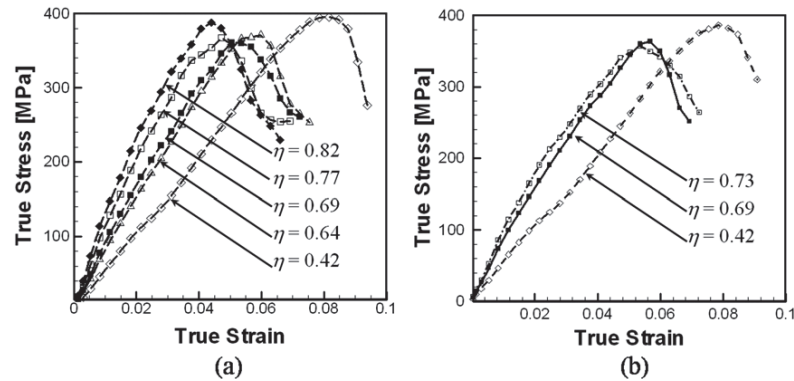


Figure 17. Comparison of calculated stress–strain curves for (a) digitized microstructures with variation of grain volume fractions (shown in figure 2) and (b) idealized microstructures (shown in figure 3) ($\eta = 0.42\text{--}0.82$, $T_i = 300\text{ K}$ and $\dot{\epsilon} = 16\,667\text{ s}^{-1}$).

the amount of heating in grains is much more significant due to transgranular fracture and subsequent frictional dissipation. This effect is more pronounced for higher grain volume fractions ($\eta = 0.77\text{--}0.82$). Calculations using idealized microstructures follow the same trend.

The stress–strain responses for digitized microstructures with variation of grain volume fractions and idealized microstructures are quantified in figures 17(a) and (b), respectively. The stress rises rapidly with strain until it reaches peak values of nearly 400 MPa before strain softening occurs. In the pre-peak regime, the response is quite sensitive to the amount of binder in the microstructures, as indicated by the slopes of the stress–strain curves. Specifically, as the binder volume fraction decreases from 0.58 to 0.18, the slope increases from 5.15 to 9.52 GPa. The relationship between the binder volume fraction (η') and the slope of the stress–strain curves (s), can be approximated by a linear fit of the form

$$s = k \cdot \eta' + s_0, \quad (19)$$

where $k = -10.93\text{ GPa}$ and $s_0 = 11.36\text{ GPa}$. This trend applies to both digitized and idealized microstructures. Note that $\eta + \eta' = 1$.

In contrast to what is seen for the stiffness, the peak stress is quite insensitive to the binder content and is similar for all the microstructures analyzed. Obviously, failure through crack development, rather than bulk deformation, plays the deciding role in determining the strength of the materials. However, the strain at which the peak stress occurs shows a clear dependence on binder content. Specifically, as the binder content changes from 0.58 to 0.18, this strain changes from 8.16% to 4.40%. This correlation can also be described by a linear fit. A detailed analysis shows that this strain has a clear significance in quantifying the transition between heating mechanisms in the microstructures. This issue will be the topic of a future publication. Here, we only focus on the onset of frictional dissipation. Figure 18 shows the total amount of frictional dissipation in the actual microstructures as a function of time. A comparison of figure 18 and figure 17(a) shows that the initiation of frictional dissipation corresponds to the peaking of stress. This observation is supported by experimental results of Siviour *et al* [49] who reported that localization of deformation leads to cracking near the peak stress. This correlation clearly demonstrates the effects of binder volume fraction on ductility, failure and energy dissipation in PBX microstructures. The relations obtained provide guidance for the design and formulation of specific materials.

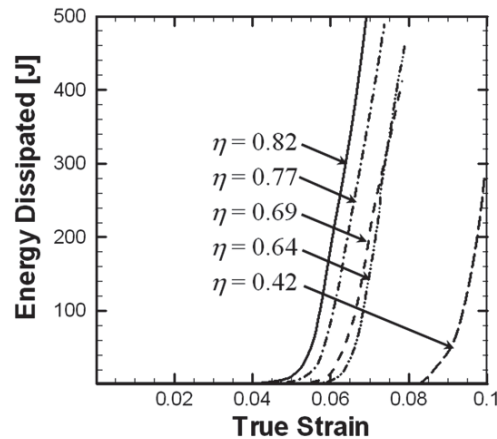


Figure 18. Frictional dissipation in the digitized microstructures with variation with grain volume fractions (shown in figure 2) ($T_i = 300$ K and $\dot{\epsilon} = 16\,667$ s $^{-1}$).

10.2. Influence of grain morphology and particle size distributions

The effect of particle shape and size has been experimentally studied in the literature. Specifically, van der Heijden [50] showed that grain content, size distribution and smoothness of grains affect the initiation pressure of RDX- and HMX-based PBXs. In this section, the CFEM framework is used to study the relative importance of the different failure mechanisms for various microstructures. A comparative study is carried out using four microstructures with different grain shapes and size distributions. The microstructures have various grain morphologies and size distributions—(A) digitized microstructure (figure 2(d)), (B) idealized microstructure with circular grains with a bimodal size distribution (figure 5(b)), (C) circular grains with a normal (or Gaussian) size distribution (figure 5(a)) and (D) diamond-shaped grains with a normal size distribution (figure 3(b)). The volume fractions of grains for all the microstructures considered are essentially the same ($\eta \approx 0.69$). Henceforth, these microstructures will be referred to as A, B, C and D.

The four microstructures (A–D) are subject to loading under conditions of nominally uniaxial stress or no lateral confinement (configuration in figure 8(b)). Figure 19 shows the distributions of temperature and microcracks in these microstructures at an overall strain of $\epsilon = 5.83\%$. All the microstructures show extensive deformation and shear banding in the binder matrix. Interfacial debonding occurs throughout the microstructures, constituting the primary mode of failure in all cases irrespective of the differences in grain morphologies and grain size distributions. Although the failure mechanism is similar among the microstructures, their stress-carrying capability as measured by the $\sigma - \epsilon$ curves differ, as shown in figure 20. At strains below approximately 2%, the curves are similar, reflecting the fact that, before the initiation of damage, the stress–strain response is determined by the composition or phase fractions. At strains beyond approximately 2%, the response varies significantly among the microstructures. While microstructures A and B exhibit higher peak stresses and higher subsequent flow stresses, microstructures C and D show lower peak stresses and gradual decreases of stress. This indicates strain softening resulting from sliding of grains and progressive damage through the development of microcracks.

Figures 21(a) and (b) show the total energy dissipated in creating crack surfaces (fracture energy) and the total energy dissipated due to the viscoelastic deformation of the binder phase

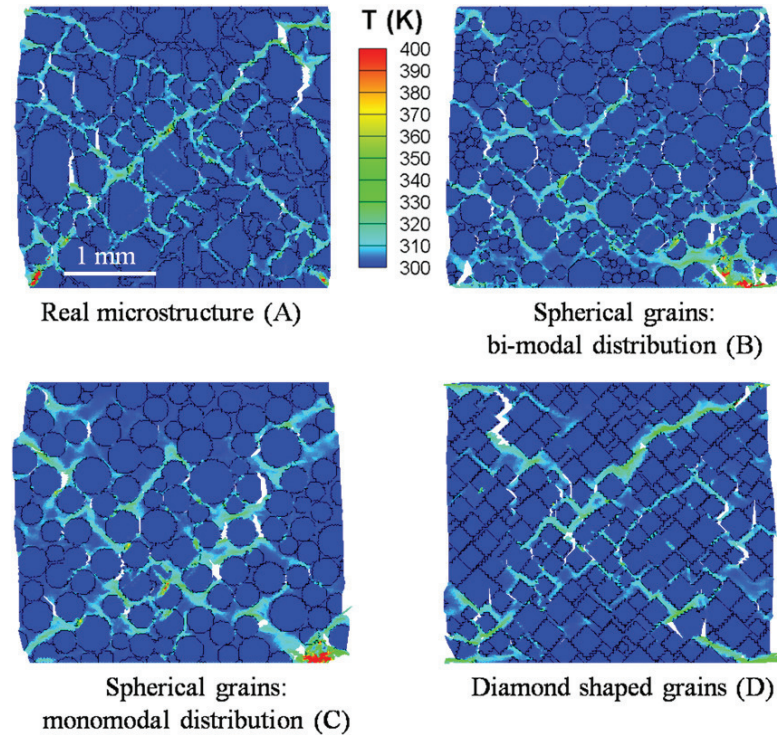


Figure 19. Distributions of temperature and damage in microstructures A–D ($T_i = 300$ K, $\dot{\epsilon} = 16667$ s $^{-1}$ and $\epsilon = 5.83\%$).

(hereafter referred to as viscoelastic dissipation), for the four microstructures A–D. Beyond a strain of 2%, fracture energy dissipations for A and B are higher than for C and D. This indicates that a higher amount of fractured surfaces is generated in the case of A and B. However, viscoelastic dissipation for microstructures A and B is lower than in the case of C and D. This can be attributed to the larger shear deformation of the binder in C and D due to enhanced sliding between grains, echoing what is seen in figure 20. This indicates that in this loading regime, strain softening in microstructures C and D is more due to sliding of grains than development of microcracks.

The difference in the post-yield response between microstructure B and microstructures C and D has to do with the distribution of grain size. In microstructures C and D (which have monomodal Gaussian grain size distributions), the packing of grains is less compact than in B, leading to larger areas of binder between adjacent grains. Consequently, more pronounced sliding can occur between granules, leading to lower overall stress levels in these microstructures and the strain softening behavior seen in figure 20. Also, the similarity in the $\sigma - \epsilon$ responses of C and D indicates that the change in grain morphology from circular to diamond does not have a significantly effect on the overall mechanical response. On the other hand, in microstructure B which has a bimodal size distribution of grains, smaller granules packed in between larger grains create interlocking arrangements of small and large grains. Such arrangements hinder sliding of grains. As a result, higher stresses develop in the microstructure. The bimodal packing also poses an obstacle to the formation

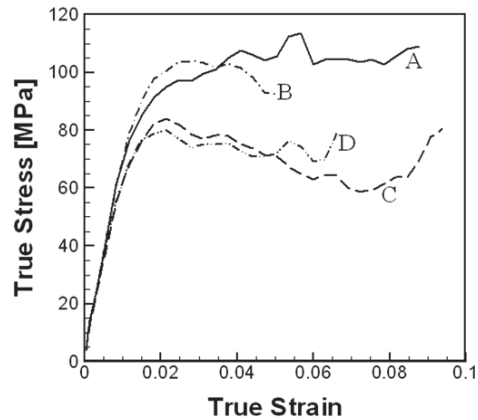


Figure 20. Comparison of stress–strain curves for microstructures with different grain morphologies ($T_i = 300\text{ K}$, $\dot{\epsilon} = 16\,667\text{ s}^{-1}$).

of large, continuous crack surfaces, partly because the tearing of the matrix requires more mechanical work than the debonding of grain–matrix interfaces as quantified by fracture energies implied by the cohesive parameters in table 2. Thus, bimodal size distributions of grains are beneficial to the load-carrying-capacity of PBXs under dynamic loading due primarily to enhanced grain–grain interactions and efficient packing of smaller grains between larger grains. Consequently, bimodal distributions are especially desirable for PBXs with higher grain volume fractions.

At the grain scale, the geometry of the particles influences the nature and severity of stress distribution and concentration. This effect in turn affects the debonding at the grain–matrix interfaces and the subsequent energy dissipation due to friction. The time histories of the total energy dissipated due to friction along crack surfaces (both along the interfaces between the two phases and inside each of the phases) for the four microstructures are shown in figures 21(c) and (d). For strains up to approximately 4%, the profiles are similar for the cases. At strains beyond 4%, higher frictional dissipation is observed for the microstructures with circular grains (B and C), followed by the microstructure with multifaceted grains (A), and the microstructure with diamond-shaped grains (D). The planar grain facets in A and D appear to facilitate interfacial debonding. At higher nominal strains, interfacial cracks coalesce, causing the constituents to separate from each other and resulting in the lateral splitting seen in figure 19. This process leads to a decrease in intergranular interactions. On the other hand, the curved interfaces associated with the circular grains in B and C make it less likely for the cracks to coalesce and the phases less likely to separate, thereby maintaining a higher level of constituent interactions and leading to higher frictional dissipation. From the point of view of designing PBXs, especially PBXs with high packing densities, multifaceted grain morphologies with planar facets may help keep frictional dissipation low under conditions with low lateral confinement or low hydrostatic pressures.

11. Concluding remarks

A fully coupled thermomechanical finite-deformation framework is developed to analyze the response of PBXs. The framework is based on the cohesive finite element method and provides explicit tracking of failure through crack development and frictional heating as well as explicit

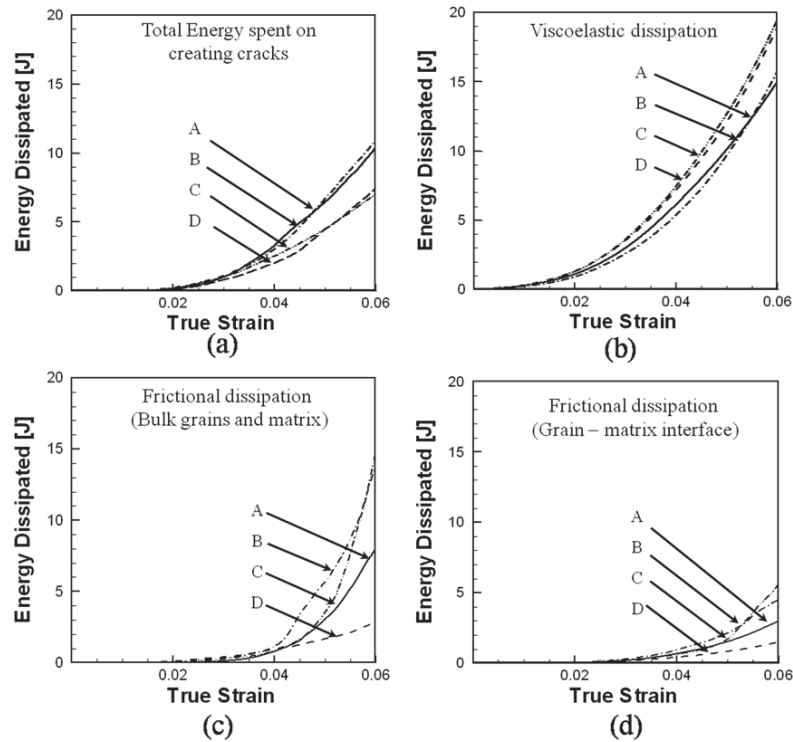


Figure 21. Histories of energy dissipation in microstructures A–D ($T_i = 300\text{ K}$, $\dot{\epsilon} = 16\,667\text{ s}^{-1}$).

account of microstructure. The analyses carried out focus on composites consisting of HMX granules bonded by an Estane matrix under conditions of deformation at strain rates on the order of $(16\text{--}17) \times 10^3\text{ s}^{-1}$. Digitized micrographs of an actual material and idealized microstructures are used to investigate the effects of composition, phase arrangement, phase size distribution and phase morphology on the evolution of temperature field, damage and failure. Calculations show that higher volume fractions of HXM granules correspond to more severe heating and a lower threshold for fracture initiation. Bimodal distributions of granule sizes are more beneficial to the mechanical integrity of the composites than monomodal distributions. Grains with planar facets increase the likelihood of failure through grain–matrix debonding relative to grains with rounded shapes. The framework developed and the results obtained are useful for developing microstructure–performance relations that can be used in the design of advanced energetic materials.

Acknowledgments

The authors gratefully acknowledge support from the Air Force Research Laboratory (AFRL) at the Eglin AFB in Florida (scientific officer: Dr Yasuyuki Horie) and the Defense Threat Reduction Agency (DTRA) (scientific officer: Dr Suhithi Peiris). This research benefited significantly from many helpful comments and suggestions from Dr Horie. Calculations are carried out on parallel computers at NAVO and the DPRL at Georgia Tech.

References

- [1] McDowell D L, Panchal J, Choi H J, Seepersad C, Allen J and Mistree F 2009 *Integrated Design of Multiscale, Multifunctional Materials and Products* (Oxford, UK: Butterworth Heinemann)
- [2] Chen P W, Huang F L and Ding Y S 2007 Microstructure, deformation and failure of polymer bonded explosives *J. Mater. Sci.* **42** 5272–80
- [3] Palmer S J P and Field J E 1982 The deformation and fracture of Beta-HMX *Proc. R. Soc. Lond. Ser. A* **383** 399
- [4] Palmer S J P, Field J E and Huntley J M 1993 Deformation, strengths and strains to failure of polymer bonded explosives *Proc. R. Soc. Lond. Ser. A* **440** 399–419
- [5] Skidmore C B, Phillips D S, Son S F and Asay B W 1998 Characterization of HMX Particles in PBX 9501 *AIP Conf. Proc.* **L29** 579–82
- [6] Liu G and Yu H 1996 Stereological characterization of particle contiguity *J. Microsc. (Oxford)* **181** 82–7
- [7] Berghout H L, Son S F, Skidmore C B, Idar D J and Asay B W 2002 Combustion of damaged PBX 9501 explosive *Thermochim. Acta* **384** 261–77
- [8] Rae P J, Goldrein H T, Palmer S J P, Field J E and Lewis A L 2002 Quasi-static studies of the deformation and failure of beta-HMX based polymer bonded explosives *Proc. R. Soc. Lond. Ser. A* **458** 743–62
- [9] Liu C 2004 Fracture of the PBX 9501 High Explosive *AIP Conf. Proc.* **706** 786–91
- [10] Williamson D M, Palmer S J P and Proud W G 2006 Fracture studies of PBX simulants materials *AIP Conf. Proc.* **845** 829–32
- [11] Gray G T III, Bluementhal W R, Idar D J and Cady C M 1998 Influence of temperature on the high strain-rate mechanical behavior of PBX 9501 *AIP Conf. Proc.* **429** 583–6
- [12] Cady C M, Blumenthal W R, Gray G T and Idar D J 2006 Mechanical properties of plastic-bonded explosive binder materials as a function of strain-rate and temperature *Polym. Eng. Sci.* **46** 812–9
- [13] Wiegand D A and Reddingius B 2005 Mechanical properties of confined explosives *J. Energetic Mater.* **23** 75–98
- [14] Siviour C R, Laity P R, Proud W G, Field J E, Porter D, Church P D, Gould P and Huntingdon-Thresher W 2008 High strain rate properties of a polymer-bonded sugar: their dependence on applied and internal constraints *Proc. R. Soc. A* **464** 1229–55
- [15] Menikoff R 2005 Elastic–plastic response of HMX Technical Report, Los Alamos National Laboratory (LA-UR-05-1500)
- [16] Benson D J and Conley P 1999 Eulerian finite-element simulations of experimentally acquired HMX microstructures *Modelling Simul. Mater. Sci. Eng.* **7** 333–54
- [17] Austin R A, McDowell D L and Benson D J 2006 Numerical simulation of shock wave propagation in spatially-resolved particle systems *Modelling Simul. Mater. Sci. Eng.* **14** 537–61
- [18] Baer M R 2002 Modeling heterogeneous energetic materials at the mesoscale *Thermochim. Acta* **384** 351–67
- [19] Menikoff R 2000 Granular explosives and initiation sensitivity *Detonation Theory & Application* T14 (special feature) Technical Report, Los Alamos National Laboratory (LA-UR-05-1500) Available at: <http://t14web.lanl.gov/Research/TDAC2000/menikoff.00.pdf>
- [20] Menikoff R 2004 Pore collapse and hot spots in HMX *AIP Conf. Proc.* **706** 393–66
- [21] Ortiz M and Pandolfi A 1999 Finite-deformation irreversible cohesive elements for three-dimensional crack-propagation analysis *Int. J. Numer. Methods Eng.* **44** 1267–82
- [22] Dwivedi S K and Espinosa H D 2003 Modeling dynamic crack propagation in fiber reinforced composites including frictional effects *Mech. Mater.* **35** 481–509
- [23] Banerjee B, Cady C M and Adams D O 2003 Micromechanics simulations of glass-estane mock polymer bonded explosives *Modelling Simul. Mater. Sci. Eng.* **11** 457–75
- [24] Wu Y-Q and Huang F-L 2009 A micromechanical model for predicting combined damage of particles and interface debonding in PBX explosives *Mech. Mater.* **41** 27–47
- [25] Needleman A 1990 An analysis of tensile decohesion along an interface *J. Mech. Phys. Solids* **38** 289–324
- [26] Tvergaard V and Hutchinson J W 1992 The relation between crack-growth resistance and fracture process parameters in elastic plastic solids *J. Mech. Phys. Solids* **40** 1377–97
- [27] Tvergaard V and Needleman A 1992 Effect of crack meandering on dynamic, ductile fracture *J. Mech. Phys. Solids* **40** 447–71
- [28] Needleman A and Tvergaard V 1994 Mesh effects in the analysis of dynamic ductile crack-growth *Eng. Fract. Mech.* **47** 75–91
- [29] Xu X P and Needleman A 1994 Numerical simulations of fast crack-growth in brittle solids *J. Mech. Phys. Solids* **42** 1397–434
- [30] Camacho G T and Ortiz M 1996 Computational modelling of impact damage in brittle materials *Int. J. Solids Struct.* **33** 2899–938

- [31] Espinosa H D, Zavattieri P D and Dwivedi S K 1998 A finite deformation continuum discrete model for the description of fragmentation and damage in brittle materials *J. Mech. Phys. Solids* **46** 1409–42
- [32] Camanho P P, Davila C G and de Moura M F 2003 Numerical simulation of mixed-mode progressive delamination in composite materials *J. Compos. Mater.* **37** 1415–38
- [33] Minnaar K and Zhou M 2002 Characterization of impact in composite laminates *AIP Conf. Proc.* **620** 1208
- [34] Zhai J and Zhou M 2000 Finite element analysis of micromechanical failure modes in a heterogeneous ceramic material system *Int. J. Fract.* **101** 161–80
- [35] Tomar V, Zhai J and Zhou M 2004 Bounds for element size in a variable stiffness cohesive finite element model *Int. J. Numer. Methods Eng.* **61** 1894–920
- [36] Rae P J, Palmer S J P, Goldrein H T, Field J E and Lewis A L 2002 Quasi-static studies of the deformation and failure of PBX 9501 *Proc. R. Soc. Lond. Ser. A* **458** 2227–42
- [37] Cady C M, Blumenthal W R, Gray G T and Idar D J 2003 Determining the constitutive response of polymeric materials as a function of temperature and strain rate *J. Physique IV* **110** 27–32
- [38] Mas E M and Clements B E 1996 A viscoelastic model for PBX binders <http://lib-www.lanl.gov/la-pubs/00818442.pdf> (LA-UR-01-3492)
- [39] Kaliske M and Rotherth H 1997 Formulation and implementation of three-dimensional viscoelasticity at small and finite strains *Comput. Mech.* **19** 228–39
- [40] Cady H H, Larson A C and Cromer D T 1963 The crystal structure of alpha-HMX and a refinement of the structure of beta-HMX *Acta Crystallogr.* **16** 617–23
- [41] Menikoff R and Sewell T D 2002 Constituent properties of HMX needed for meso-scale simulations *Combust. Theor. Modelling* **6** 103–25
- [42] Sewell T D and Menikoff R 2003 Complete equation of state for Beta-HMX and implications for initiation *AIP Conf. Proc.* **706**
- [43] Mas E M, Clements B E and George D C 2004 Direct numerical simulations of PBX 9501 *AIP Conf. Proc.* **706** 389–92
- [44] Skidmore C B, Philips D S, Assay B W, Idar D J, Howe P M and Bolme D S 2000 Microstructural effects in PBX-9501 damaged by shear impact *AIP Conf. Proc.* **505** 659–62
- [45] Zhai J, Tomar V and Zhou M 2004 Micromechanical simulation of dynamic fracture using the cohesive finite element method *J. Eng. Mater. Technol.—Trans. ASME* **126** 179–91
- [46] Tan H, Liu C, Huang Y and Geubelle P H 2005 The cohesive law for the particle/matrix interfaces in high explosives *J. Mech. Phys. Solids* **53** 1892–917
- [47] Zhou M, Needleman A and Clifton R J 1994 Finite-element simulations of shear localization in plate impact *J. Mech. Phys. Solids* **42** 423–58
- [48] Peters J F, Muthuswamy M, Wibowo J and Tordesillas A 2005 Characterization of force chains in granular material *Phys. Rev. E* **72** 041307
- [49] Siviour C R and Proud W G 2007 Damage formation during high strain rate deformation of PBS9501 *AIP Conf. Proc.* **955** 799–802
- [50] van der Heijden A, Bouma R H B and van der Steen A C 2004 Physicochemical parameters of nitramines influencing shock sensitivity *Propellants Explosives Pyrotech.* **29** 304–13